Available online at www.sciencedirect.com
ScienceDirect
Journal of the European Ceramic Society 30 (2010) 641–648
www.elsevier.com/locate/jeurceramsoc

Confocal fluorescence microscopy in alumina-based ceramics: Where does the signal come from?

Sheng Guo [a], Richard I. Todd *

University of Oxford, Department of Materials, Parks Road, Oxford OX1 3PH, United Kingdom

Received 25 June 2009; received in revised form 20 August 2009; accepted 24 August 2009
Available online 7 October 2009

Abstract

Confocal Cr^{3+} fluorescence microscopy is an ideal technique for investigating residual stresses in alumina-based ceramics. Due to their transparency, however, it is important to understand where the collected signal comes from by characterising the probe response function (PRF). Here, a PRF is proposed that captures all the relevant physical effects, including a newly identified consequence of scattering by pores and grain boundaries. The new PRF describes the response of a range of alumina-based ceramics to depth scanning in a high resolution confocal fluorescence microscope in a manner that balances physical significance with the accuracy of empirical fitting. The results showed that measurements could be made deep within single crystals of sapphire and ruby, although refraction degraded the depth resolution from about 3 μm at the surface to 25 μm at a depth of 500 μm. Scattering and absorption limited the depth to which polycrystalline alumina could be probed to ∼15 μm. This was further reduced to ∼4 μm for an alumina–10 vol.% SiC nanocomposite. However, the absorption increased the accuracy of near surface measurements in these materials by preventing contamination from subsurface fluorescence.

Keywords: Al_2O_3; Residual stress; Spectroscopy; Fluorescence microscopy

1. Introduction

Characterisation of residual stresses caused by thermal expansion mismatch,[1–4] indentation[5] or machining induced residual stress[6–8] is an important issue in ceramics. It is crucial to a better understanding of procedures such as the indentation fracture toughness test[9,10] and to understanding the effect of the residual stresses on crack initiation and propagation and hence on mechanical performance.

Residual stresses in ceramics have previously been investigated by curvature measurement (for machining stresses),[7] X-ray diffraction,[3,11] neutron diffraction,[4] cathodoluminescence microscopy (CLM)[12–14] and photoluminescence microscopy (PLM).[1–5,15,16] PLM involves the illumination of the specimen by a laser focused through the objective lens of an optical microscope. The light collected by the same objective includes both directly scattered or reflected laser light and luminescence, resulting from interaction of the incident photons with phonons (the Raman effect) or electrons in the material (e.g. Cr^{3+} fluorescence in chromium-doped alumina-based ceramics.[17,18] The wavelength of many luminescent lines in the spectrum is sensitive to stress; stress measurements can therefore be made by analysing the spectrum using a diffraction grating and calibrating the peak shift with respect to stress. When implemented using a confocal microscope to improve the depth and lateral resolution, PLM has higher spatial resolution than all other techniques except for CLM so that local stress variations are sampled as well as the mean stress. PLM is also less time-consuming and more cost effective than other techniques.

Owing to the transparency of some ceramics, a significant proportion of the signal collected in PLM comes from beneath the surface of the specimen even when the microscope is focused at the surface. This provides the potentially advantageous ability to probe subsurface stresses, but also complicates the analysis and interpretation of results, which are averaged over a three dimensional volume with a weighting according to the variation of illumination and collection efficiency. The depth resolution is always worse than the lateral resolution and for many cases

* Corresponding author. Tel.: +44 1865 273718.
E-mail address: richard.todd@materials.ox.ac.uk (R.I. Todd).
[a] Current address: Department of Mechanical Engineering, The Hong Kong Polytechnic University, Hung Hom, Kowloon, Hong Kong.

0955-2219/$ – see front matter © 2009 Elsevier Ltd. All rights reserved.
doi:10.1016/j.jeurceramsoc.2009.08.020

the resolution can usefully be characterised by the axial probe response function (PRF) alone,[19] the PRF being the distribution function describing the contribution to the spectral intensity of a given axial position (or depth) within the probe volume. For many examples of interest (e.g. grinding, polishing, indentation, thermal stresses in coatings and composites) the stresses vary over length scales comparable to the axial resolution of the microscope so it is essential for this to be taken into account if quantitative stress measurements are to be interpreted correctly.

There are several previous papers dealing with the spatial origin of the PLM signal in transparent or semi-transparent ceramics. Lipkin and Clarke[20] have presented a detailed account of the effects of stress distributions on the profile and position of spectral lines in a weakly confocal microscope using an essentially transparent material (ruby). Much of the subsequent literature modifies this approach to take into account other factors, not considered by Lipkin and Clarke. Atkinson et al.,[21] for instance, considered semi-transparent materials and added an absorption factor to Lipkin and Clarke's Lorentzian PRF to account for the attenuation of the illumination and collected luminescence in such materials. In transparent materials, Everall[22,23] pointed out that refraction at the specimen surface leads to a degradation of the axial resolution that increases in proportion to the depth below the surface of the focal plane. This approach was extended substantially by Baldwin and Batchelder[24] who separated the illumination and collection volumes for confocal microscopes and derived analytical expressions for their axial response. This approach gives substantial physical insight into the variation of collected intensity and resolution as the focal plane of the objective is moved through the specimen surface. Bruneel et al.[25] investigated Baldwin and Batchelder's model experimentally and suggested semi-empirical modifications to describe the PRF more accurately for practical use.

Most of the above works have focused on the technique itself. Other papers have used similar approaches to investigate specific sources of residual stress in ceramics.[26,27] These have required only those refinements to the simple approach of Lipkin and Clarke[20] that are appropriate to the specific application. The current paper addresses a particular class of material rather than details of the technique or a particular source of residual stress. The materials considered are all based on aluminum oxide, the most widely used structural ceramic, and range from single crystals to polycrystalline composites. These have been investigated using the Cr^{3+} fluorescence peaks in the photoluminescence spectrum of alumina;[17,18] almost all nominally pure alumina specimens contain sufficient Cr^{3+} impurity for these peaks to be collected easily. One objective is to ascertain the maximum depth below the surface of such materials that can sensibly be probed when the degradation in resolution, scattering and absorption are considered, in order to provide a guide to the type of problem to which PLM can be applied. This has required all of the refinements to Lipkin and Clarke's original approach reviewed above to be taken into account, and a new modification to account for scattering has also been found necessary. The second objective of the work is to provide a general PRF for use in residual stress investigations of alumina-based materials by Cr^{3+} fluorescence microscopy. The approach is "semi-empirical" in that we use physically derived results to guide the development of the PRF as far as is possible, but modify these empirically where necessary to ensure a good description of the results for practical application.

2. Experimental

2.1. Materials and specimen preparation

Single crystals of sapphire and ruby, pure polycrystalline alumina and alumina/SiC nanocomposites containing 2–10 vol.% SiC were used to provide contrasting examples of alumina-based materials. For examples of single crystals, a 400 μm thick sapphire with surface orientation of $(1\,\bar{1}\,0\,2)$ (*r*-plane) and two pieces of ruby with surface orientations of (0 0 0 1) (*c*-plane) and $(1\,1\,\bar{2}\,0)$ (*a*-plane) and thicknesses of 500 and 530 μm respectively were used.

The procedure for preparing the polycrystalline alumina and Al_2O_3/SiC nanocomposites followed our previous work.[28] The starting powders were AKP50 alumina (200 nm, Sumitomo, Japan, 99.995% purity) and UF45 SiC (260 nm, Lonza, Germany, contains 0.2% free Si, 0.6% free C and 3.5% oxygen) respectively. 0.25 wt.% MgO was added to prevent abnormal grain growth. Mechanical mixing by attrition milling (Szegvari HD, USA) using YSZ milling media was performed at a speed of 300 rpm for 2 h. The ratio of water to powder was 4:1 by volume and 2.1% of the weight of solid of Dispex A40 (Allied Colloids, UK) was used as a dispersant. The mixture was freeze dried (Edwards Micromodulyo, UK) for 24 h. The powder was passed through a 150 μm sieve and then calcined at 600 °C for 1 h to remove organics. Hot pressing in a graphite die was used to produce dense specimens. A pressure of 25 MPa was applied in an argon atmosphere with a dwell time of 30 min at maximum temperatures between 1450 and 1700 °C, to give materials of similar alumina grain size (5–8 μm).

All specimens were sequentially polished to a 1 μm diamond surface finish. For sapphire and ruby specimens, both top and bottom surfaces were polished.

2.2. Cr^{3+} fluorescence measurements

The fluorescence microscopy experiments were performed using a confocal Raman microscope (System 1000, Renishaw, UK) and incident radiation from a 633 nm He–Ne laser. A 100× lens with a numerical aperture of 0.9 was used. The confocal aperture in the instrument is formed by the intersection of two slits at 90° to one another. One is a physical slit, which in the experiments described here was set to 10 μm. The other slit is virtual and is formed by using only a narrow stripe of pixels in the CCD camera used for collecting the diffraction pattern from the grating used to analyse the luminescent spectrum. The width of this stripe was set to 2 pixels in our experiments, which gives a virtual slit width corresponding to the 10 μm width of the real slit at 90° to it.

The basic experiment in this work is the "depth scan" in which the motorised specimen stage of the instrument is used to step

the focal plane of the lens through the surface of the specimen, collecting luminescent spectra at each step. When performing a depth scan, the laser was first focused on the sample surface. Displacements of the motorised stage from this position and normal to the surface are termed Δz, in this work, with positive Δz such that the focal plane moves into the specimen. To perform the scan, the stage was first moved to a negative value of Δz, and then moved in steps of 1 μm so that the focal plane went from above to below the specimen surface. The exposure time was 20 s per point.

The R1 peak intensity, I, was determined by fitting the spectra with two pseudo-Voigt peaks (one for the R1 peak and one for the overlapping R2 peak) using the commercial fitting software, Grams/32 (Galactic Industries, USA).

The adjustable parameters of the PRF models proposed in Section 3 were determined from the best fit of the PRF models to the experimental data. The curve fitting was carried out using the commercial software package, OriginPro (OriginLab, USA).

3. Experimental results and PRF modeling

The variation of R1 peak intensity, I, with the displacement of the sample surface relative to the objective lens, Δz, is plotted for all specimens in Fig. 1. Some of the effects requiring modification of Lipkin and Clarke's Lorentzian PRF described in Section 1 are immediately apparent. The strong attenuation of the collected intensity when focusing below the surface of the polycrystalline specimens demonstrates their relative opacity, for example, and Everall's refraction induced degradation[22,23] is apparent as a sharper transient in intensity as the probe enters the sapphire specimen than when it emerges at the bottom surface. The accurate representation of all these effects requires a large number of adjustable parameters, and although many of these have clear physical interpretations, simultaneous fitting of all of them would be mathematically indeterminate. We therefore build up our model PRF systematically, beginning with sapphire, the simplest material, and then adding further terms to the basic PRF to describe the additional effects found in other materials.

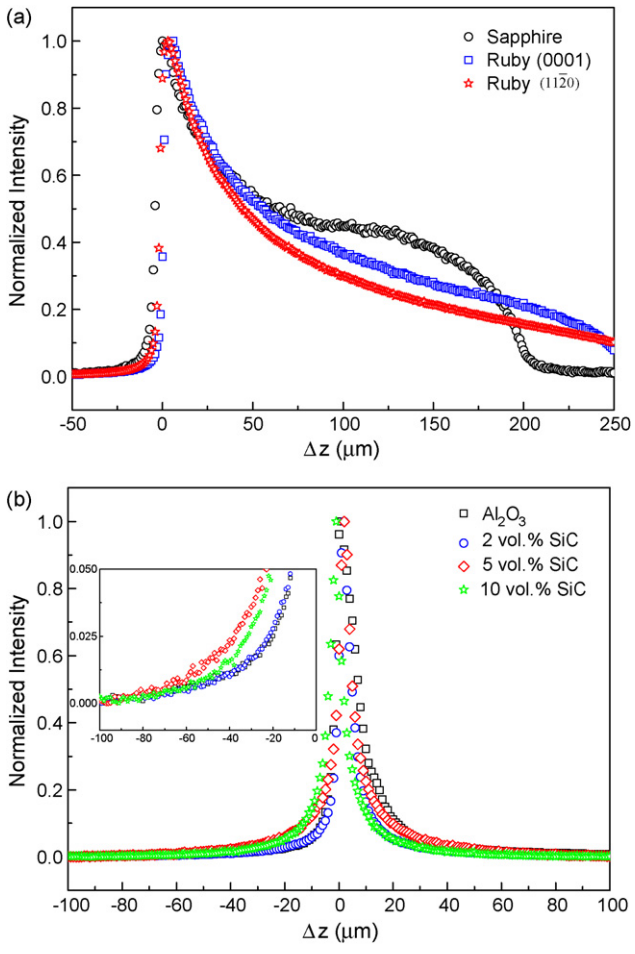

Fig. 1. Experimental intensity-through-depth curves for (a) single crystal sapphire and ruby specimens and (b) polycrystalline alumina and Al_2O_3/SiC nanocomposites. The inset in (b) shows an enlargement of the $\Delta z < 0$ tail.

3.1. PRF for sapphire and ruby

Lipkin and Clarke[20] used a simple Lorentzian to describe the PRF of a weakly confocal microscope. With this assumption, the R1 peak intensity, I, is related to the translation of the microscope stage, Δz, by the following expressions:

$$I(z_0) \propto \int_0^t \frac{p}{(z - z_0)^2 + p^2}\,\mathrm{d}z \tag{1}$$

where

$$z_0 = n\Delta z \tag{2}$$

and t is the thickness of the sample, p is the probe half length, z_0 is the distance between the focal plane and the sample surface and n is the refractive index of the specimen. Note in Eq. (1) that a function of the form $p/(p^2 + z^2)$ is used instead of the conventional Lorentzian, $p^2/(p^2 + z^2)$. This is because both functions are Lorentzian in shape, but the integral of the former over infinite or semi-infinite limits is a constant ($\pi/2$ for a half space) while the latter is dependent on p. The use of the form in Eq. (1) allows p to be varied without changing the predicted intensity when z_0 is either zero or deep within the material.

Eq. (1) can be integrated analytically. For a 400 μm thick sapphire, the intensity profile as the probe moves from above the top surface, through the specimen and out of the bottom surface is shown in Fig. 2, for a representative value of p. The refractive index for sapphire is 1.8.[21] There is a big discrepancy between the theory and the experimental data for sapphire shown in Fig. 1(a).

This is known to be caused by several related consequences of refraction at the air/sample interface, which is more complicated than the simple change in the depth of focal plane expressed in Eq. (2). Everall[22] used a ray-tracing analysis to investigate the effect of refraction on the axial resolution of confocal Raman microscopy. The analysis showed that rays passing through the lens at different radii from the central axis are brought to a focus at different depths below the specimen surface owing to refraction (rays further from the axis come to focus deeper in the specimen than is suggested by Eq. (2)). This decreases the

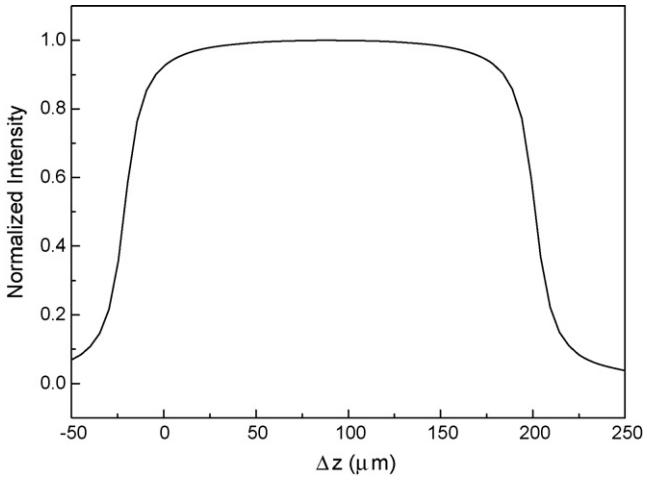

Fig. 2. Prediction of the depth scan line shape for sapphire from Eq. (5).

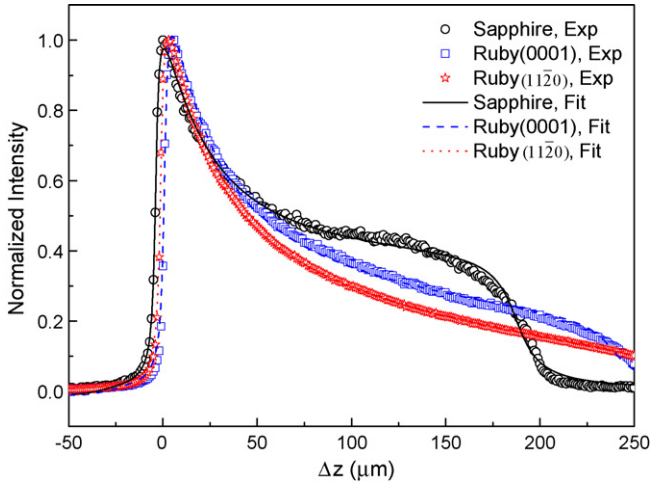

Fig. 3. Fitting results of the PRF model represented by Eqs. (5) and (6) to the experimental data for sapphire and ruby. "Exp" and "Fit" in the legend denote the experimental data and fits to the equations respectively. The same symbols apply for the subsequent plots. Note that the working distance of the lens did not allow values of $\Delta z > 250\,\mu m$ to be investigated.

axial resolution of the microscope in proportion to Δz and is apparent in our results for sapphire in Fig. 1(a) as was noted above.

A second effect of refraction for a strongly confocal microscope such as ours is that it affects the collection of the luminescent radiation from the sample. Baldwin and Batchelder's detailed analysis[24] suggests this to be responsible for the sharp reduction in intensity after the probe has entered the top surface of the specimen. Bruneel et al.[25] investigated Baldwin and Batchelder's model experimentally and while many of the model's predictions were borne out qualitatively, some disagreement was found when quantitative comparisons were made. Bruneel et al. suggested that this is because Baldwin and Batchelder had only considered the axial intensity in their analysis, an exact treatment of off-axis effects being intractable, and suggested semi-empirical modifications to describe the PRF more accurately.

Our model for the probe depth incorporates these modifications as follows. First, we replace the true refractive index, n, in Eq. (2) with an effective refractive index, k_1, which is expected to be slightly greater than n owing to Everall's prediction that marginal rays come to focus deeper in the specimen than axial rays, which obey Eq. (2). We assume the degradation of axial resolution to be linear with nominal depth of focus, as suggested by Everall[22] and supported by Baldwin and Batchelder[24] so that the probe length, p, becomes:

$$p = k_2 + k_3 \Delta z \tag{3}$$

where k_2 is the axial resolution at the sample surface and k_3 is the linear broadening coefficient.

To allow for the effect of refraction on the collection efficiency, Bruneel et al.[25] suggested a correction to Baldwin and Batchelder's analysis involving the divergence of the lens, and therefore its numerical aperture (Eq. (10) of Ref. 25). Although this considerably improves the fit to experiment, the initial drop after the probe enters the specimen is not well modeled (Fig. 5 of Ref. 25) and we therefore resort to the following empirical factor to describe the intensity collected by the confocal aperture as a function of probe depth:

$$H(\Delta z) = (1 - k_6)\frac{k_4^2}{k_4^2 + (\Delta z - k_5)^2} + k_6 \tag{4}$$

where k_4, k_5 and k_6 are adjustable parameters.

Incorporating these ideas, Eq. (1) becomes:

$$I(\Delta z) = k_8 \int_0^t \left[(1 - k_6)\frac{k_4^2}{k_4^2 + (\Delta z - k_5 - k_7)^2} + k_6\right] \times \frac{k_2 + k_3(\Delta z - k_7)}{([k_2 + k_3(\Delta z - k_7)]^2 + [z - k_1(\Delta z - k_7)]^2)}\,\mathrm{d}z \tag{5}$$

where k_7 is the offset of the $z = 0$ plane due to the practical difficulty in focusing the laser on the sample surface before the depth scans and k_8 is the intensity normalising parameter to match the results to the experimental intensity.

The eight parameters in Eq. (5) were adjusted to fit the experimental data for sapphire in Fig. 1 and a satisfactory fitting was achieved, as shown in Fig. 3. The fitted parameters are listed in Table 1. These show that the effective refractive index, k_1, is 2.1, slightly greater than the true refractive index, $n = 1.8$, as expected; the axial resolution on the sample surface is 2.9 μm, which is very close to the value of 2.6 μm obtained directly by measuring the breadth of the collected intensity peak as the probe is scanned through the surface of an essentially opaque specimen of silicon;[29] the offset of the $z = 0$ plane position, k_7, is less than 4 μm which is the approximate uncertainty in focusing the laser on the surface of a transparent material. Different fitting strategies showed that the other, more empirical parameters were very reproducible and mathematically stable.

The high chromium content in ruby leads to significant absorption of the radiation so for describing these specimens we follow Atkinson et al.[21] in using an exponential absorption

Table 1
List of fitting parameters for sapphire and ruby specimens.

Material	k_1	k_2 (μm)	k_3	k_4 (μm)	k_5 (μm)	k_6	k_7 (μm)	k_8	k_9 (μm^{-1})
Sapphire	2.09	2.88	0.0886	21.0	−36.2	0.101	−3.67	1.20	0
Ruby[a]	2.09	2.88	0.0886	21.0	−36.2	0.101	0.981	1.27	0.000670
Ruby[b]	2.09	2.88	0.0886	21.0	−36.2	0.101	−1.02	1.28	0.00110

[a] (0 0 0 1).
[b] (1 1 $\bar{2}$ 0).

term to allow for this:

$$I(\Delta z) = k_8 \int_0^t e^{-2k_9 z} \left[(1-k_6) \frac{k_4^2}{k_4^2 + (\Delta z - k_5 - k_7)^2} + k_6 \right] \times \frac{k_2 + k_3(\Delta z - k_7)}{([k_2 + k_3(\Delta z - k_7)]^2 + [z - k_1(\Delta z - k_7)]^2)} \, \mathrm{d}z \quad (6)$$

where k_9 is the absorption coefficient. As this is expected to be the only significant difference from the sapphire experiment, the other parameters were those already fitted to the sapphire result with the exception of k_7, the focus offset, and k_8, the intensity normalising parameter, for obvious reasons. The resulting agreement with experiment was very good for both ruby specimens, as shown in Fig. 3. The absorption coefficient, k_9, of the (1 1 $\bar{2}$ 0) ruby was higher than that of the (0 0 0 1) ruby (Table 1) because of its higher chromium content, which was shown by its darker colour. This demonstrates the physical significance of this parameter.

3.2. PRF for alumina and Al_2O_3/SiC nanocomposites

In principle, Eq. (6) can also be applied using the values for k_1–k_6 established for sapphire to describe the experimental data for the more opaque polycrystalline alumina and Al_2O_3/SiC nanocomposites, essentially by adjusting the absorption coefficient, k_9 (plus the offset and normalising parameters k_7 and k_8 as usual). Fig. 4 shows that the fit obtained is indeed excellent in the main part of the peaks for such materials, again supporting the basic approach. However, the fitting in the tails is not satisfactory and this suggests that some information is missing from the PRF function, Eq. (6). Close inspection of the intensity–depth curves shown in Fig. 1(b) shows that for $\Delta z > 0$ (probe below the surface), the collected intensity decreases more quickly for the nanocomposites than for the alumina, as might be expected owing to the stronger absorption resulting from the SiC inclusions. However, for $\Delta z > 0$ (probe centre above the surface) the 5 and 10 vol.% SiC nanocomposites give a *stronger* signal than alumina (see inset to Fig. 1(b)), which is not consistent with this argument. Similarly, the fits in Fig. 4 for both the nanocomposites and the alumina underestimate the collected intensity for $\Delta z < 0$. A plausible explanation for these effects is that the opacity of polycrystalline alumina and the nanocomposites is partly caused be *elastic scattering* of light by pores, grain boundaries and (in the nanocomposites) SiC particles rather than true *absorption*.[30] The scattering could make the intensity–depth curves broader as both the illuminated volume and the collection volume would be blurred by this effect, thus degrading the resolution. This blurring would be stronger in the nanocomposites than in alumina owing to the extra effect of the SiC particles, as observed. It is difficult to account for the scattering analytically but given that scattering is strongest in the forward direction, so that the distance travelled in the material for singly scattered photons, and thus the absorption, is similar to that for unscattered beams it seems reasonable to describe the detection of scattered radiation by simply adding a second Lorentzian term of the form of Eq. (1) but with a greater probe length, k_{10}:

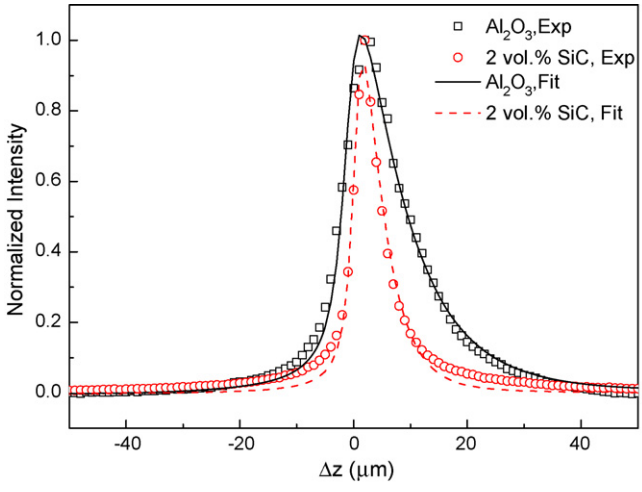

Fig. 4. Fitting results of the PRF model represented by Eq. (6) to the experimental data for Al_2O_3 and 2 vol.% Al_2O_3/SiC nanocomposite.

$$I(\Delta z) = \int_0^t e^{-2k_9 z} \left[k_{11} \frac{k_2}{k_2^2 + [z - k_1(\Delta z - k_7)]^2} + k_{12} \frac{k_{10}}{k_{10}^2 + [z - k_1(\Delta z - k_7)]^2} \right] \mathrm{d}z \quad (7)$$

where k_{11} and k_{12} represent the relative contributions from unscattered and scattered radiation to the intensity. Because of the small penetration depth in these materials, the degradation of the resolution (k_3) and the $H(\Delta z)$ function (Eq. (4)) that accounts for the different collected intensity at different depths have been ignored.

Eq. (7) was used to fit the experimental data for alumina and Al_2O_3/SiC nanocomposites and very good fittings were achieved, as shown in Fig. 5 and the fitting parameters are given in Table 2. Note that k_1 and k_2 are not adjustable parameters in Eq. (7): they are the fitted values for sapphire (Table 1). Clearly, k_9 and k_{12} should be connected—stronger scattering contributes to a higher value of k_9 and should also increase the relative

Table 2
List of fitting parameters for Al_2O_3 and Al_2O_3/SiC nanocomposites.

Material	k_7 (μm)	k_9 (μm^{-1})	k_{10} (μm)	k_{11}	k_{12}	k_{12}/k_{11}
Al_2O_3	−0.871	0.0403	71.6	0.605	0.221	0.365
2 vol.% SiC	0.527	0.104	36.2	0.890	0.560	0.629
5 vol.% SiC	0.924	0.143	29.5	0.955	1.809	1.89
10 vol.% SiC	−1.713	0.305	16.1	1.29	3.34	2.59

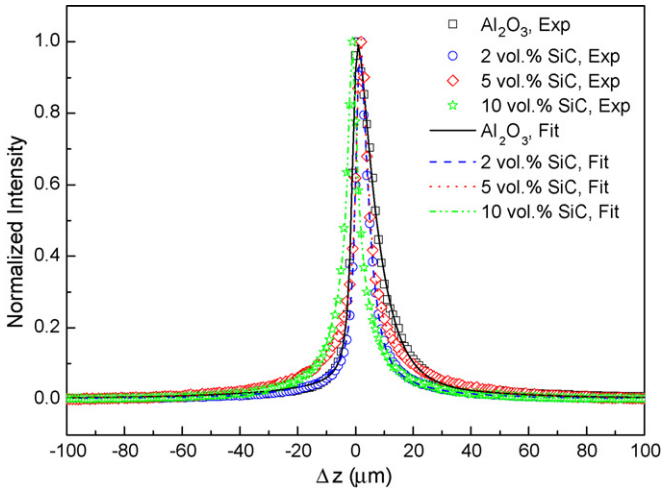

Fig. 5. Fitting results of the PRF model represented by Eq. (7) to the experimental data for Al_2O_3 and x vol.% Al_2O_3/SiC nanocomposites ($x = 2, 5, 10$).

contribution of the scattering Lorentzian, k_{12}. Table 2 confirms this monotonic relationship between them but the mathematical form of this connection is not currently understood and hence these parameters were fitted separately. The excellent fit is to be expected mathematically simply from the effectively increased number of adjustable parameters. However, we note that the fitted absorption coefficients of nanocomposites are higher than that of alumina, and increase with the SiC content and the relative contribution from scattering to the intensity, k_{12}/k_{11}, also increases with the SiC content. This suggests that the parameters k_{10}, k_{11} and k_{12} are physically meaningful though it is clear that further work is needed on this area.

4. Discussion

4.1. Physical significance of the PRF model

It is tempting to be suspicious of a fit involving so many apparently adjustable parameters but it should be stressed that in the basic PRF, Eq. (6), only k_4–k_6 are truly empirical. All the other parameters have clear physical interpretations and the fitted values are consistent with the expected values. Furthermore, each of these other parameters is mathematically well defined because each describes one particular feature of the curve. The relationship between the thickness of the crystal and the value of Δz at which the intensity reduces due to the emergence of the probe at the bottom surface of the crystal, is solely determined by the effective refractive index, k_1; the initial rise in intensity as the probe enters the top surface by the innate probe length, k_2, and the corresponding reduction in resolution on exit by k_3. We conclude that the basic model has an appropriate balance between being sufficiently physically informed to capture the main features of the PRF and sufficiently adjustable to give accurate fits. We will shortly publish papers demonstrating its useful application to residual stress problems in alumina-based materials.

4.2. How far below the surface of alumina-based ceramics can we probe?

Fig. 6 shows our estimated axial resolution, expressed as the probe half width p, as a function of probe depth using Eq. (3). Although the degradation with depth from the value of ∼3 μm at the surface is significant, the resolution of ∼25 μm at a depth of 500 μm is still good enough to be useful in many applications. In order for such subsurface measurements to be made in practice, however, the effect of absorption must also be considered; not only must there be sufficient collected intensity from the measurement depth to be detected, but also it must represent a significant fraction of the total collected intensity, so that it dominates the spectrum recorded and is not affected by luminescence from other depths.

In order to assess this, the percentage of the total collected intensity coming from the nominal resolution range $(z_0 - p \le z \le z_0 + p)$ has been calculated as a function of the focal

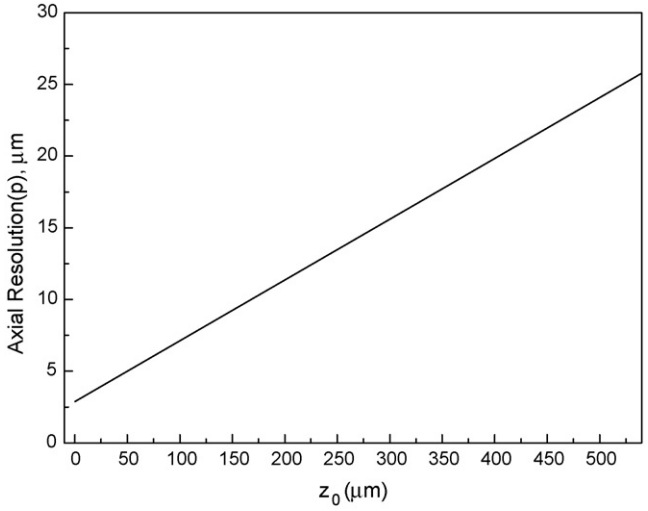

Fig. 6. Degradation of axial probe resolution (p) with depth in alumina-based ceramics.

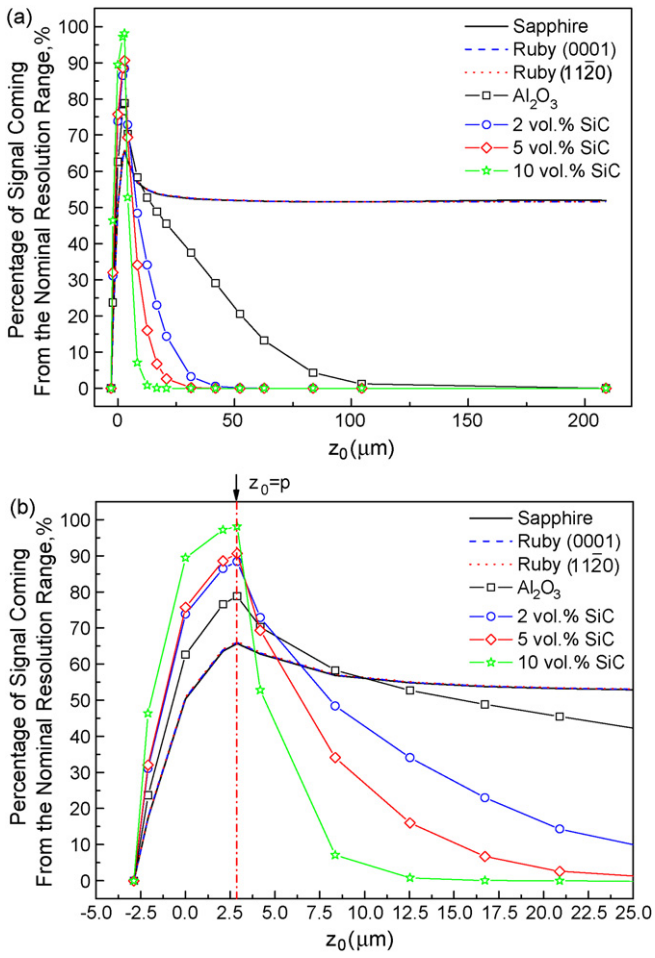

Fig. 7. (a) Percentage of signal coming from the nominal resolution range around the focal depth z_0 as a function of nominal focus depth, z_0. (b) Enlarged region near the surface in (a) and the dotted line indicates the maximum $I_{z_0\pm p}\%$ position.

depth, z_0:

$$I_{z_0\pm p}\% = 100 \times \frac{\int_{z_1}^{z_2} f(z)\,\mathrm{d}z}{\int_0^t f(z)\,\mathrm{d}z} \tag{8}$$

where p is the resolution half length at z_0 as defined by Eq. (3); $f(z)$ is the modified Lorentzian function as defined in Eqs. (6) and (7) according to the material; $z_1 = z_0 - p$ when $z_0 - p \geq 0$ or $z_1 = 0$ when $z_0 - p < 0$; $z_2 = z_0 + p$ when $z_0 + p \leq t$ or $z_2 = t$ when $z_0 + p > t$.

The results are shown in Fig. 7 for the ceramics investigated. $I_{z_0\pm p}\%$ is maximum at $z_0 = p$ for all the materials, as would be expected for a simple Lorentzian in a transparent material. This shows that the most accurate measurements are made with the probe focused just below the surface, rather than on it.

The nearly transparent sapphire and ruby specimens all follow the same line. The maximum $I_{z_0\pm p}\%$ is ~66%, again as for a Lorentzian in a transparent material, and it then decreases slowly and reaches a nearly constant value of ~52%, close to the corresponding Lorentzian/transparent materials limit of 50%. Taking $I_{z_0\pm p}\% \geq 50\%$ as an arbitrary condition for meaningful measurements, it is clear that there is no inherent problem in achieving stress measurements with the depth resolution shown in Fig. 6 for single crystal specimens.

Owing to their strong absorption/scattering, the situation is somewhat different for the polycrystalline alumina and nanocomposites. The maximum depth that can be probed meaningfully according to the above criterion is ~15 μm for the alumina, and only ~4 μm for the 10% SiC nanocomposite. While this prevents measurements from significant depths being made, there are advantages to the absorption and scattering in these materials: the maximum $I_{z_0\pm p}\%$ values for Al_2O_3/x vol.% SiC ($x = 0, 2, 5, 10$) are 79%, 88%, 91% and 98%, respectively. This indicates that higher resolution measurements can be made at the surface of such materials, especially the nanocomposites, because the absorption prevents the adulteration of the signal by the portion of the PRF far from the centre. Finally, the differences between the response of alumina and the nanocomposites shows that care must be taken when comparing these materials using PLM, as the effective source volume of the signal varies significantly between them. This will be the subject of a future publication.

5. Summary

A PRF model for confocal photoluminescence microscopy of alumina-based ceramics has been proposed in this work that draws on various publications in the literature to capture relevant effects, including the consequences of refraction at the specimen surface. In addition, a method of accounting for the elastic scattering found to affect the results has been proposed. The model was found to fit the results of intensity vs. depth scans for a wide range of alumina ceramics with mathematical robustness and consistency with the physical meaning of the adjustable parameters involved. The results showed that the innate resolution of the confocal instrument used deteriorated from ~3 μm when focused at the surface of the specimen to ~25 μm when focused 500 μm below the surface of sapphire. When using polycrystalline specimens, however, accurate measurements could not be made at such depths owing to the effects of scattering and absorption. The maximum probable depth for polycrystalline alumina was ~15 μm, and for an alumina–10 vol.% SiC nanocomposite it was only ~4 μm.

Acknowledgements

The authors thank Dr. Apichart Limpichaipanit of the University of Oxford for providing the polycrystalline alumina and Al_2O_3/SiC nanocomposite specimens. S Guo would like to thank the KC Wong Education Foundation and the Overseas Research Students Awards Scheme for the financial support for his D. Phil study at the University of Oxford.

References

1. Ma, Q. and Clarke, D. R., Piezospectroscopic determination of residual stresses in polycrystalline alumina. *Journal of the American Ceramic Society*, 1994, **77**, 298.

2. Ortiz Merino, J. L. and Todd, R. I., Thermal microstress measurements in Al_2O_3/SiC nanocomposites by Cr^{3+} fluorescence microscopy. *Journal of the European Ceramic Society*, 2003, **23**, 1779.
3. Levin, I., Kaplan, W. D. and Brandon, D. G., Residual stresses in alumina–SiC nanocomposites. *Acta Metallurgica Et Materialia*, 1994, **42**, 1147.
4. Todd, R. I., Bourke, M. A. M., Borsa, C. E. and Brook, R. J., Neutron diffraction measurements of residual stresses in alumina/SiC nanocomposites. *Acta Materialia*, 1997, **45**, 1791.
5. Molis, S. E. and Clarke, D. R., Measurement of stresses using fluorescence in an optical microprobe: stresses around indentations in a chromium-doped sapphire. *Journal of the American Ceramic Society*, 1990, **73**, 3189.
6. Zhao, J., Stearns, L. C., Harmer, M. P., Chan, H. M. and Miller, G. A., Mechanical behavior of alumina–silicon carbide 'nanocomposites'. *Journal of the American Ceramic Society*, 1993, **76**, 503.
7. Chou, I. A., Chan, H. M. and Harmer, M. P., Machining-induced surface residual stress behavior in Al_2O_3–SiC nanocomposites. *Journal of the American Ceramic Society*, 1996, **79**, 2403.
8. Tanner, B. K., Wu, H. Z. and Roberts, S. G., Direct evidence for compressive elastic strain at ground surfaces of nanocomposite ceramics. *Applied Physics Letters*, 2005, 86.
9. Anstis, G. R., Chantikul, P., Lawn, B. R. and Marshall, D. B., A critical evaluation of indentation techniques for measuring fracture-toughness. 1. Direct crack measurements. *Journal of the American Ceramic Society*, 1981, **64**, 533.
10. Chantikul, P., Anstis, G. R., Lawn, B. R. and Marshall, D. B., A critical evaluation of indentation techniques for measuring fracture-toughness. 2. Strength method. *Journal of the American Ceramic Society*, 1981, **64**, 539.
11. Tanner, B. K., Wu, H. Z., Roberts, S. G. and Hase, T. P. A., Subsurface damage in alumina and alumina–silicon carbide nanocomposites. *Philosophical Magazine*, 2004, **84**, 1219.
12. Ostertag, C. P., Robins, L. H. and Cook, L. P., Cathodoluminescence measurement of strained alumina single crystals. *Journal of the European Ceramic Society*, 1991, **7**, 109.
13. Pezzotti, G., Leto, A., Tanaka, K. and Sbaizero, O., Piezo-spectroscopic assessment of nanoscopic residual stresses in Er^{3+}-doped optical fibres. *Journal of Physics-Condensed Matter*, 2003, **15**, 7687.
14. Todd, R. I., Stowe, D., Galloway, S., Barnes, D. and Wilshaw, P. R., Piezospectroscopic measurement of the stress field around an indentation crack tip in ruby using SEM cathodoluminescence. *Journal of the European Ceramic Society*, 2008, **28**, 2049.
15. Banini, G. K., Chaudhri, M. M., Smith, T. and Hayward, I. P., Measurement of residual stresses around Vickers indentations in a ruby crystal using a Raman luminescence microscope. *Journal of Physics D-Applied Physics*, 2001, **34**, L122.
16. Wu, H. Z., Roberts, S. G. and Derby, B., Residual stress distributions around indentations and scratches in polycrystalline Al_2O_3 and Al_2O_3/SiC nanocomposites measured using fluorescence probes. *Acta Materialia*, 2008, **56**, 140.
17. Ma, Q. and Clarke, D. R., Optical fluorescence from chromium ions in sapphire—a probe of the image stress. *Acta Metallurgica Et Materialia*, 1993, **41**, 1811.
18. He, J. and Clarke, D. R., Determination of the piezospectroscopic coefficients for chromium-doped sapphire. *Journal of the American Ceramic Society*, 1995, **78**, 1347.
19. Ma, Q. and Clarke, D. R., Measurement of residual stresses in sapphire fiber composites using optical fluorescence. *Acta Metallurgica Et Materialia*, 1993, **41**, 1817.
20. Lipkin, D. M. and Clarke, D. R., Sample-probe interactions in spectroscopy: sampling microscopic property gradients. *Journal of Applied Physics*, 1995, **77**, 1855.
21. Atkinson, A., Jain, S. C. and Webb, S. J., Convolution of spectra in optical microprobe experiments. *Semiconductor Science and Technology*, 1999, **14**, 561.
22. Everall, N. J., Modeling and measuring the effect of refraction on the depth resolution of confocal Raman microscopy. *Applied Spectroscopy*, 2000, **54**, 773.
23. Everall, N. J., Confocal Raman microscopy: why the depth resolution and spatial accuracy can be much worse than you think. *Applied Spectroscopy*, 2000, **54**, 1515.
24. Baldwin, K. J. and Batchelder, D. N., Confocal Raman microspectroscopy through a planar interface. *Applied Spectroscopy*, 2001, **55**, 517.
25. Bruneel, J. L., Lassegues, J. C. and Sourisseau, C., In-depth analyses by confocal Raman microspectrometry: experimental features and modeling of the refraction effects. *Journal of Raman Spectroscopy*, 2002, **33**, 815.
26. Zhu, W. L. and Pezzotti, G., Spatially resolved stress analysis in Al_2O_3/3Y-TZP multilayered composite using confocal fluorescence spectroscopy. *Applied Spectroscopy*, 2005, **59**, 1042.
27. Bridges, T. E., Houlne, M. P. and Harris, J. M., Spatially resolved analysis of small particles by confocal Raman microscopy: depth profiling and optical trapping. *Analytical Chemistry*, 2004, **76**, 576.
28. Todd, R. I. and Limpichaipanit, A., Microstructure–property relationships in wear resistant alumina/SiC "nanocomposites". *Advances in Science and Technology*, 2006, **45**, 555.
29. Guo, S. and Thesis:, PhD., *Fluorescence Microscopy Investigation on Residual Stresses in Alumina-based Ceramics*. University of Oxford, 2009.
30. Jenkins, F. A. and White, H. E., *Fundamentals of Optics*. McGraw-Hill, New York; London, 1976.